This is the author's version (manuscript) of the work that was accepted for publication in Applied Thermal Engineering
The Version of Record is available online at https://doi.org/10.1016/j.applthermaleng.2022.118092

Experimental validation of a CFD model to simulate the heat transfer in shell-and-tube, moving packed-bed heat exchangers

Julian D. Hertel*, Stefan Zunft

Institute of Engineering Thermodynamics, German Aerospace Center, Pfaffenwaldring 38-40, Stuttgart, Germany

Abstract

Shell-and-tube, moving-bed heat exchangers could offer a promising solution to generate steam in particle-based solar towers, where they need to withstand high pressure and a wide temperature spread. To provide guidance during the design stage, accurate and time-efficient simulation tools are required that are capable of capturing the complex heat transfer characteristics of this type of heat exchanger.

In this article, we present a comprehensive set of thermal models to simulate the heat transfer in a moving bed heat exchanger with horizontal tubes. The model builds upon previous works in which we proposed a 2D multiphase continuum approach for more time-efficient computation. Simulations were experimentally validated by using specially prepared measuring probes that allowed us to resolve and compare the local heat transfer coefficients around the tube circumference.

The comparison showed that simulated heat transfer coefficients match the experimental data in general, but also suggest that the implemented thermal models slightly overestimate the influence of the stagnation and the void zone.

Keywords: Moving bed heat exchanger, Particle, Continuum model, Particle Image Velocimetry, Concentrating solar power

* Corresponding Author
E-Mail addresses: julian.hertel@dlr.de (J. D. Hertel), stefan.zunft@dlr.de (S. Zunft)

1 Introduction

Concentrating solar power (CSP) could play an important role during the global transition towards a more renewable and sustainable energy supply. One promising prospect for next generation CSP plants are solar towers that operate with ceramic particles in the primary circuit. Using granular material as a working fluid comes with two major advantages over conventional systems. First, the exceptional thermal stability of the bulk allows the plant to be operated at unprecedented temperature levels potentially exceeding 1000 °C; thereby increasing the overall efficiency and reducing the levelized cost of energy of the system. Second, particles can simultaneously be used as a storage material. By integrating an adequately sized bin, from which bulk can be drawn on demand, the plant is effectively made suitable for covering baseload demand.

One key component of particle-based solar towers is the heat exchanger, in which heat is transferred from the primary to the secondary loop. Extracting heat from the bulk is a challenging task due to its extremely low thermal diffusivity. In recent years, different designs of gravity-driven moving bed heat exchangers (MBHE) have been proposed as an alternative to more mature but costly fluidized bed technologies. For example, Albrecht and Ho published multiple studies on the development of the MBHE that is to be installed in the G3P3 project [1-3]. They opted for a shell-and-plate design to transfer heat from the particles into highly pressurized CO_2-microchannels. Other studies looked into designs with horizontal tubes as, e.g., in [4, 5] and [6]. One benefit of this more traditional tube bundle design is that it is relatively mature and robust, which made it the primary choice for the steam generator in the HIFLEX pilot-plant project, in which very demanding temperature drops across the heat exchanger of more than 600°C (300°C–950°C) are targeted [7].

MBHEs, in general, show flow and heat transfer characteristics that differ notably from conventional technologies. This is why accurate simulation tools are needed to provide guidance during the design phase. In a shell-and-plate heat exchanger, it is safe to assume plug flow allowing the application of more simplified, straight-forward numerical models such as explored in [8]. The particle flow field in MBHEs with horizontal tubes, on the other hand, is comparatively more complex. There has been one attempt by Niegsch et al. [6] to capture this complexity in a fully analytical model, however, the model does not take into consideration neither the temperature dependence of the thermophysical properties of the bulk nor the continuously changing tube wall temperatures across the MBHE. Note that in [9] and [10] the thermal conductivity of granular media was reported to depend strongly on its temperature. Therefore, in the case of large temperature drops between the inlet and the outlet, Niegsch' model presents too much of an over-simplification to be considered for the real case application, and it is eventually necessary to resort to more accurate models based on computational fluid dynamics (CFD) or the discrete element method (DEM).

DEM simulations have been applied in various occasions to gain a better understanding of the flow field and heat transfer in MBHEs. Mentionable examples are Guo et al. [11], who studied the impact of oscillating horizontal tubes; Guo et al. [12], who tried to identify certain characteristics of the granular flow around a single tube; and Tian et al. [13], who calculate the heat transfer coefficients around tubes of different shape. All of these studies were restricted to analysing the flow around a single tube. The reason for this is that, despite today's computing capacity, DEM simulations still take up a significant amount of CPU time. This means that, although DEM simulations are useful to analyse and optimize certain isolated design features, they are still too time consuming to simulate the MBHE as a whole.

Contrary to DEM, CFD simulations do not numerically integrate the equations of motion for every single particle, but instead treat granular media as a continuum, this way translating the soil mechanics into an Eulerian context. As a result, CFD simulations can be more time efficient and offer an interesting alternative for solving the energy balance of the MBHE system as a whole within a reasonable time frame and without losing much of the accuracy of DEM simulations. This led us to believe that a multiphase continuum model could fill an important gap in the portfolio of simulation tools, which are necessary to reduce design costs and ultimately help to pave the way towards commercialized particle-based solar towers.

A first foundation for such a model has been laid in our previous works [14] and [15]. There, the authors set up a 2D-multiphase continuum model of the particle flow inside a MBHE with horizontal tubes and compared the simulated flow field with DEM simulations to validate the underlying rheological models. With the validity of the momentum equations established, it is the purpose of this study to take it one step further and validate the implemented heat transfer models (Section 2) by comparing simulations with experimental results (Section 3 and 4).

2 Heat transfer models

The simulation model discussed in this article is based on the Eulerian multiphase approach, in which the gas phase (dry air) and the solid phase (particles) of the bulk are treated as interpenetrating continua.

This means that for each phase a separate set of momentum and energy equations with their respective material properties is solved.

As the rheological models, which are part of the momentum equations, have already been presented and validated in previous works [14, 15], only the underlying thermal models will be discussed herein. All models have been implemented in ANSYS FLUENT 2019 R3.

We begin with the thermal energy transport equation, which constitutes the basis of all following models. As an example, Eq. (1) shows an essential extract from the ANSYS FLUENT manual [16] for the solid phase — whereas the correlation for the gas phase follows the same pattern.

$$\frac{\delta}{\delta t}(\varepsilon_s \rho_s h_s) + \nabla(\varepsilon_s \rho_s \boldsymbol{u}_s) = \nabla \cdot \left(\lambda_{eff,s} \nabla T\right) + \alpha_{sg} A_i \left(T_s - T_g\right) \tag{1}$$

In our case, energy transport is dominated by convection, diffusion (first term on the RHS), and heat transfer between the phases (second term on the RHS). To characterize these terms, meaningful assumptions need to be made about the effective thermal conductivity of the bulk, λ_{eff}, and the interphase exchange coefficient, α_{sg}, respectively.

To describe the effective thermal conductivity of the bulk, we opted for the model of Zehner, Bauer and Schluender, often referred to as the ZBS model. This model was first published in [17, 18] and works on the presumption that the complexity of the bulk can be reduced to the heat transfer mechanisms taking place in a single representative unit cell. The model has been validated and implemented in many studies such as [2, 19, 20] and has proven its usefulness to this day. While for the exact correlation the interested reader is directed to the original publications or to [21], Eq. (2) only focuses on the key input parameters of the effective thermal conductivity.

$$\lambda_{eff} = f(\, \varepsilon_g, p, T, d_s, \varphi_s, C_{f,s}, \varepsilon_s, \rho_s, \lambda_s, c_{p,g}, \rho_g, \lambda_g, \varepsilon_b') \tag{2}$$

ε_g is the voidage of the packed bed, p is the gas pressure, and T is the temperature. The remaining parameters in Eq. (2) are more closely described in Table 1, along with their corresponding values as implemented in this study.

The ZBS model was originally developed to describe the heat transfer in fixed packed beds and does not include convective heat transfer from one phase to another at the presence of slip velocity. To account for convection, a term α_{sg} must be defined describing the heat transfer between the phases. A definition for α_{sg} between a fluid and spherical particles was given by Gunn [22] (see Eq. (3)).

$$Nu_{sg} = \frac{\alpha_{sg} d_s}{\lambda_g} = \left(7 - 10\varepsilon_g + 5\varepsilon_g^2\right)\left(1 + 0.7Re^{0.2}Pr^{1/3}\right) + \left(1.33 - 2.4\varepsilon_g + 1.2\varepsilon_g\right)Re^{0.7}Pr^{1/3} \tag{3}$$

where Re and Pr are the Reynolds and Prandtl number of the gas phase and d_s is the mean particle diameter.

Regarding the tube walls, considerable effort has been put into the modelling of the boundary conditions. Previous research has shown that heat transfer between a surface and the bulk involves a thermal contact resistance, α_c^{-1}, due to a reduced packing fraction near the wall. This contact resistance leads to a temperature drop proportional to α_c according to Eq. (4) and Fig. 1.

$$\dot{q} = \alpha_c(T)\left(T_w - T_w^{mod}\right) \tag{4}$$

The modelling of the experiment in Section 3 requires a constant heat flux, $\dot{q}$, from the surface into the bulk. It is then possible to derive the wall temperature of the tubes if the contact resistance α_c is known. Different formulations of the contact resistance have been proposed in the past, for example, Albrecht and Ho [8] used the model of Botterill and Denoyle [23]. In this case, we implemented the contact resistance model of Tsotsas [24] (see Eq. (5)).

$$\alpha_c = \underbrace{\varphi\alpha_{WP}}_{wall-particle} - \underbrace{(1-\varphi)\alpha_g}_{voidage\ (gas)} + \underbrace{\alpha_{rad}}_{radiation} \tag{5}$$

where φ is the particle coverage at the wall. It represents the ratio of the projected area of particles in contact with the wall to the overall area of the wall. According to Tsotsas, heat transfer directly from the surface can be divided into three parts: 1) direct heat transfer from the wall to contacting particles, α_{WP}, 2) convective heat transfer through gaps in the adjacent particle layer, α_g, and 3) heat transfer by radiation, α_{rad}.

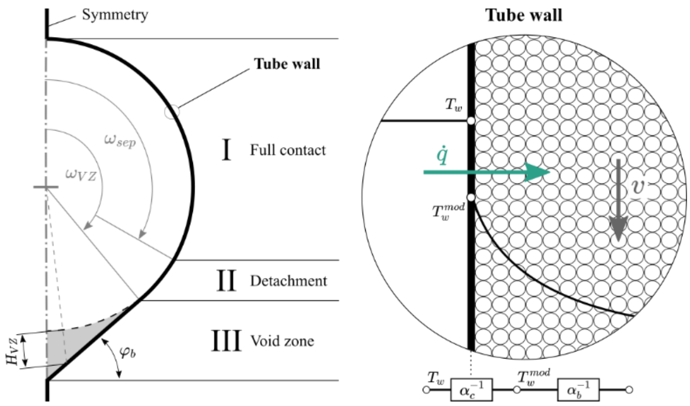

Fig. 1 Different regions along the tube wall to model the temperature drop ($T_w - T_w^{mod}$) in Eq. (5).

Initially, Eq. (5) was proposed to model the temperature drop observed in bulk flow along a plane surface. However, gravity-driven bulk flow around the profile of a horizontal tube exhibits some unique phenomena that had to be accommodated in simulations. In principle, the tube boundary can be divided into the three different regions depicted in Fig. 1. Each region includes a different set of modifications to Eq. (5).

Region I ($\omega < \omega_{sep}$): Full contact

At the upper part of the tube ($\omega < \omega_{sep}$) particles are in full contact with the wall. In this region it is assumed that the coverage factor is at a constant value $\varphi_0 = 0.65$. This value is based on an educated guess.

Region II ($\omega_{sep} < \omega < \omega_{VZ}$): Detachment

When approaching a critical angle ω_{sep} in the converging part of the flow channel, particles quickly start to separate from the wall. It is important to include this phenomenon in the form of a steeply decreasing coverage factor $\varphi(\omega)$. In doing so, the contact resistance in Eq. (5) is increasingly dominated by heat transfer through gaps, while direct heat transfer between particles and the wall is diminished. Bartsch performed a series of DEM simulations to derive the empiric expression in Eq. (6) giving the coverage factor in the transition region $\omega_{sep} < \omega < \omega_{VZ}$ [25]:

$$\varphi(\omega) = 0.5\varphi_0 \left\{ \tanh\left[\frac{4\left(\omega - 0.5\omega_{sep} - 0.5\omega_{VZ}\right)}{\omega_{VZ} - \omega_{sep}}\right] - 1 \right\} \tag{6}$$

According to this function, the coverage factor decreases from φ_0 to 0 within the interval $\omega_{sep} < \omega < \omega_{VZ}$.

Region III ($\omega > \omega_{VZ}$): Void zone

At the angular position ω_{VZ}, particles will have separated completely and will create some space between the tube wall and the bulk flow, called the void zone. We would like to point out, here, that the void zone is supposed to arise naturally in the flow field as a solution of solving the momentum equations. Unfortunately, this ended up not being the case, as reported in [14]. Despite considerable simulation efforts, the void zone continued to collapse with time, which is why it was finally modelled as part of the boundary conditions. Note that somehow similar numerical problems were reported in [26].

As experimental results in Section 4 will show, heat transfer in the void zone decreases significantly. With $\varphi = 0$, the coefficient α_c in Eq. (5) is now completely reduced to air convection, α_g, and radiation, α_{rad}. Tsotsas [24] already provided an expression for α_g ($\alpha_{g,ZBS}$). This expression is valid for those parts of the wall that are fully or partly in contact with the bulk, but the theory breaks down closer to the void zone. Here, heat transfer needs to be described with a different coefficient, $\alpha_{g,VZ}$ (see Eq. (7)).

$$\alpha_g = \begin{cases} \alpha_{g,ZBS} & \text{for } \omega < \omega_{VZ} \\ \varphi_g \alpha_{g,ZBS} - \left(1 - \varphi_g\right)\alpha_{g,VZ} & \text{for } \omega > \omega_{VZ} \end{cases} \tag{7}$$

In order to transition smoothly from $\alpha_{g,ZBS}$ to $\alpha_{g,VZ}$, a linearly decreasing weighting factor, φ_g, was included with

$$\varphi_g = \frac{\omega - \pi}{\omega_{VZ} - \pi} \tag{8}$$

For $\alpha_{g,VZ}$ in the void zone, Niegsch et al. [27] used the expression in Eq. (9). It had originally been proposed by Churchill and Chu to model the heat transfer by natural convection along a vertical wall [28].

$$\alpha_{g,VZ} = \frac{\lambda_g}{H_{VZ}(\omega)} \left[0.825 + \frac{0.387 Ra^{1/6}}{[1 + (0.437/Pr)^{9/16}]^{8/27}}\right]^2 \tag{9}$$

where Ra and Pr are the Rayleigh and Prandtl number of the gas phase inside the void zone. H_{VZ} is the characteristic length defined as the radial distance between the tube wall and the bulk, as indicated in Fig. 1.

Fig. 2 will help to gain a better understanding of Eq. (5) to (9) by illustrating a set of curves that is characteristic of the heat transfer along the tube wall. Within the transition zone (Region II), the factor φ causes the overall heat transfer, α_c, to decrease rapidly as the bulk separates from the wall. Within the void zone (Region III), $\alpha_{g,ZBS}$ slowly transitions towards $\alpha_{g,VZ}$. This complex nature of the contact resistance α_c^{-1} will play an important role in the interpretation of the results discussed in Section 4.

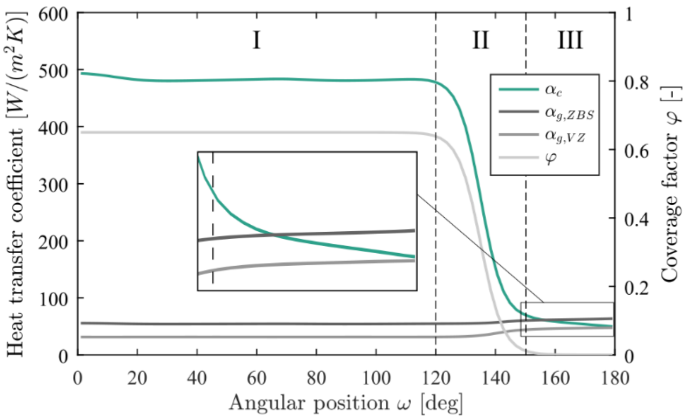

Fig. 2 Different heat transfer coefficients and coverage factor along the tube wall with $\omega_{sep} = 120°$ and $\omega_{VZ} = 150$.

Now that all of the implemented thermal models have been laid out, it is important to choose a reasonable set of input parameters with regard to the experiments in the next section. For our tests, we used the CarboCeramics Carbobead HSP 20/40 particles with a mean diameter of approximately $700\ \mu m$. Table 1 highlights the important properties of this product along with the corresponding input parameters for model characterization. Parameters are based on data from the particle manufacturer, the literature, standardized preliminary measurements, or heuristic estimations from preceding DEM simulations.

Table 1 Properties of the CarboBead HSP 20/40 sample for the characterization of the presented thermal models

Property	**Value/Correlation**	**Unit**	**Source**
Air			
Thermal conductivity $\lambda_g(T)$	Table (piecewise-linear)	W/(Km)	[29]
Density $\rho_g(T)$	Table (piecewise-linear)	Kg/m3	[29]
Specific heat capacity $c_{p,g}(T)$	Table (piecewise-linear)	J/(kgK)	[29]
Bauxite			
Thermal conductivity $\lambda_s(T)$	$\lambda_s = 6 \times 10^{-8} \cdot T^2 - 2 \times 10^{-4} \cdot T + 2.176$	W/(Km)	[10]
Density ρ_s	3600	Kg/m3	Measured/manufacturer
Specific heat capacity $c_{p,s}(T)$	$c_{p,s} = -1.15 \times 10^{-4} \cdot T^2 + 0.3989 \cdot T + 778$	J/(kgK)	[10]
Surface roughness	1E-6	-	estimate

Mean diameter d_s	700	μm	manufacturer
Form factor φ_s	0.0077 (sphere)		[18]
Form factor $C_{f,s}$	1.25 (sphere)		[18]
Bulk			
Angle of repose φ_b	32	deg	Measured
Inner angle of friction φ_i	30	deg	Measured
Emissivity ε_b'	0.9 (rough sand)	-	[30]
Heuristic parameters			
Emissivity wall	0.1 (polished steel)	-	[30]
Coverage φ_0	0.65	-	From DEM
Separation angle ω_{sep}	120	deg	[25]
Void zone angle ω_{VZ}	150 (=180-φ_b)	deg	[25]

3 Experimental approach and setup

Local heat transfer coefficients (HTC) were measured using the small heat exchanger mockup shown in Fig. 3. The mockup is consists of fifteen horizontal dummy tube rows and is placed inside a particle circulatory system, which was presented in previous studies [15, 31]. During operation, cold particles flow, driven by gravity, from an elevated storage container through the mockup, while the mass flux is controlled with a rotary valve at the bottom. A chain conveyer constantly removes the bulk from underneath the valve and returns it to the storage container to guarantee a stable particle supply and a steady flow field.

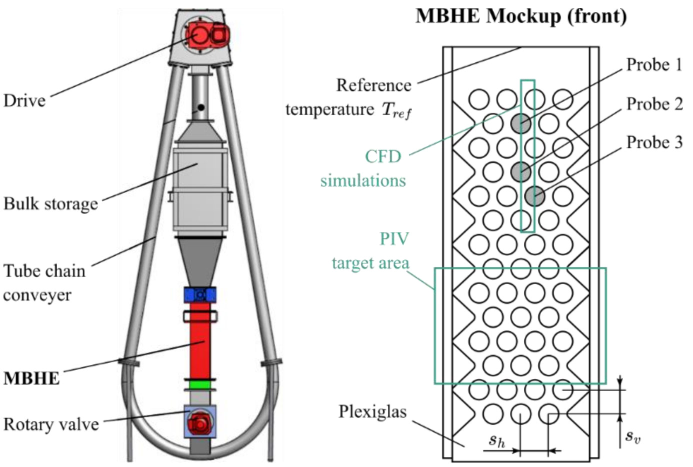

Fig. 3 Particle circulatory system (left) and heat exchanger mockup (right) with three measuring tubes

Tests were conducted at the four different velocities listed in Table 2. These mean velocities refer to an average across the inlet area of the mockup and correlate to the mass flux according to Eq. (10).

$$\bar{v}_i = \frac{\dot{m}_i}{\rho_b A_{in}} \tag{10}$$

where ρ_b is the density of the bulk, and A_{in} is the inlet cross-sectional area. As mentioned before, the mass flux $\dot{m}$ depends on the position of the rotary valve. Prior to testing, the valve had been carefully calibrated by temporarily redirecting the particle flow directly below the valve into a catch bin and monitoring the collected mass over time.

Local HTCs were measured at three different positions in the second, fourth and fifth tube row, as indicated in Fig. 3. At these locations, the dummy tubes were replaced by the specially prepared measuring probes illustrated in Fig. 4. The probes were made of a temperature-resistant polyethylene (PE) tube with a thin steel foil wrapped around it. During measurements, the foil is electrically heated by applying a constant electric current. The released heat per surface area can be calculated according to Eq. (11).

$$\dot{q} = J^2 \rho t \tag{11}$$

where J is the electric current per cross-sectional area perpendicular to the current paths, ρ is the electrical resistivity of the foil, and t is the thickness of the foil. Eq. (11) is based on the premise that the generated volumetric heat will be transferred entirely towards the bulk, and that heat transfer through the PE pipe as well as thermal redistribution within the foil are negligible. With this definition of $\dot{q}$, a local HTC, $\alpha(\omega)$, at a specific angular point, ω, on the outer tube surface can be defined with the following equation.

$$\alpha(\omega) = \frac{\dot{q}}{T_w(\omega) - T_{ref}} \tag{12}$$

where T_{ref} is the reference temperature measured at the inlet of the mockup (see Fig. 3), and $T_w(\omega)$ is the temperature at a specific angular position ω (see Fig. 4). The wall temperature $T_w(\omega)$ is measured with thermocouples, which are firmly located inside notches in the axial direction and only their tips are in contact with the foil at the center of the tube. To obtain HTCs at different angular positions, ω, the probes were successively turned in steps of 10°. As each probe carries three thermocouples, the temperature profile, $T_w(\omega)$, around the entire perimeter could be covered more quickly.

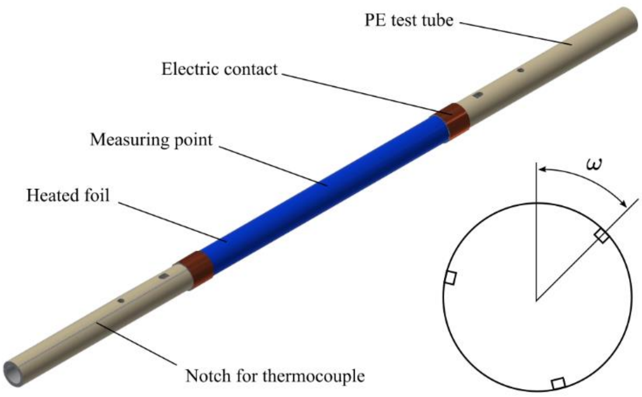

Fig. 4 Heated measuring probes used to measure the local heat transfer coefficents

Table 2 gives a summary of the relevant geometrical and operational parameters for the tests. The electric current was fixed to $I = 28.0$ A for all test sequences to prevent wall temperatures from exceeding 130°C at any given point. It was assumed that high temperatures could affect the effectiveness of the adhesive and lead to undesired detachment of the foil. With the electric current set to $I = 28.0$ A, the constant surface heat flux is $\dot{q} = 3370\ \mathrm{W/m^2}$ based on Eq. (11).

Prior to measurements, multiple tests had been conducted to determine the uncertainty of the results discussed in Section 4. Those tests included:

- measuring both the electrical resistivity of the foil and its uncertainty
- calibrating the valve positions with their corresponding mass flow rates
- measuring the homogeneity of the temperature field across the heated foil
- checking the response of the thermocouples and their contact with the foil

In addition to the thermal analysis, a camera was positioned in front of the mockup to measure the flow field by means of particle image velocimetry (PIV). Both the front and the back of the mockup were made of plexiglass to allow for an unobstructed observation of the granular flow, with the camera pointing at the lower part of the mockup (see Fig. 3).

Table 2 Geometrical and operational parameters for the tests

Parameter	**Value**	**Unit**	**Uncertainty (absolute)**	**Uncertainty (relative) [%]**
Inlet area of mockup A_{in}	633.6	cm^2		
Vertical spacing s_v	39.4	mm		
Horizontal spacing s_h	34.12	mm		
Tube diameter D	27.0	mm		

Foil perimeter P	84.82	mm	1.0	1.18
Foil thickness t	0.025	mm	0.0025	10.0
Foil resistivity ρ	7.73×10^{-7}	Ωm	1.13×10^{-9}	0.147
Electric current I	28.0	A	0.1	0.357
Current density J	1.32×10^{7}	A/m^2		
Heat flux (Eq. (11))	3370	W/m^2		13.7
Mass flows	[138, 344, 551, 758]	g/s		3.3
Velocities (Eq. (10))	[1.0, 2.5, 4.0, 5.5]	mm/s		

4 Comparison of CFD simulations with experimental results

In this section, experimental results will be compared to CFD simulations based on the thermal models covered in Section 2. By assuming symmetry in the horizontal direction, the simulation domain can be reduced to a small channel that includes the three heated measuring probes demonstrated in Fig. 3. Fig. 5 illustrates exemplary simulation results of the temperature and velocity field for a constant outlet velocity of $\bar{v} = 1.0\ \mathrm{mm/s}$ and surface heat flux of $\dot{q} = 3370\ \mathrm{W/m^2}$ from the probes P1, P2 and P3.

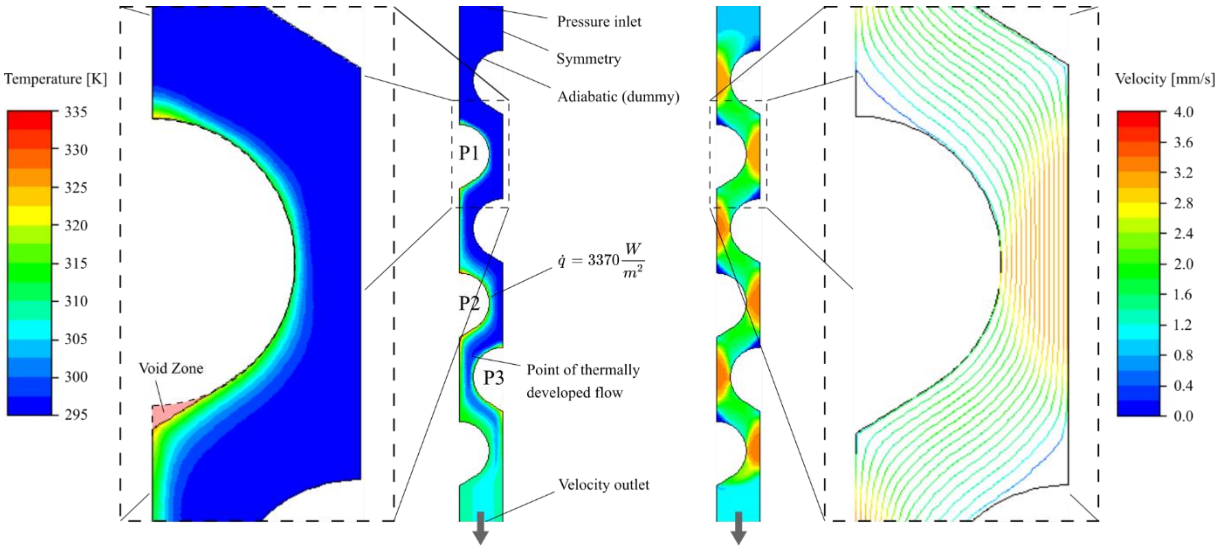

Fig. 5 CFD temperature field (left) and flow field (right) for an outlet velocity of 1 mm/s. Simulations are based on the thermal models and parameters in Section 2, the flow region is also indicated in Fig. 3.

As can be seen, the velocity field is fairly periodic in the flow direction. Simulations clearly capture the formation of the stagnation zone manifesting itself as an area of highly reduced velocities on top of the tubes. It is due to these low velocities that the stagnation zone acts like a small insulation layer and diminishes the heat transfer in this region. Furthermore, note that the flow field is very orderly, which in turn will affect temperature field. In regions where the bulk is in contact with a heated surface, a thermal boundary layer develops and will grow with increasing residence time. Since no significant mixing takes place, this boundary layer is mainly preserved in the streamwise direction and will impair the heat transfer at successive tube rows in an accumulating manner.

Fig. 6 reports the circumferential HTCs based on measurements at the velocities stated in Table 2. Results were derived from measured wall temperatures, $T_w(\omega)$, reference temperatures, T_{ref}, at the inlet of the mockup, and Eq. (12). Test results suggest that HTCs stay mainly constant up to an angle of $\omega = 90°$. Typically, for an unseparated flow of a Newtonian fluid around a cylinder, highest HTCs could be expected at the top of the tube, where the thermal boundary still had no time to develop and driving temperature gradients are high. In the case of non-Newtonian particle flow, however, it seems that otherwise enhanced heat transfer in this region is compensated by the insulation effect of the stagnation zone.

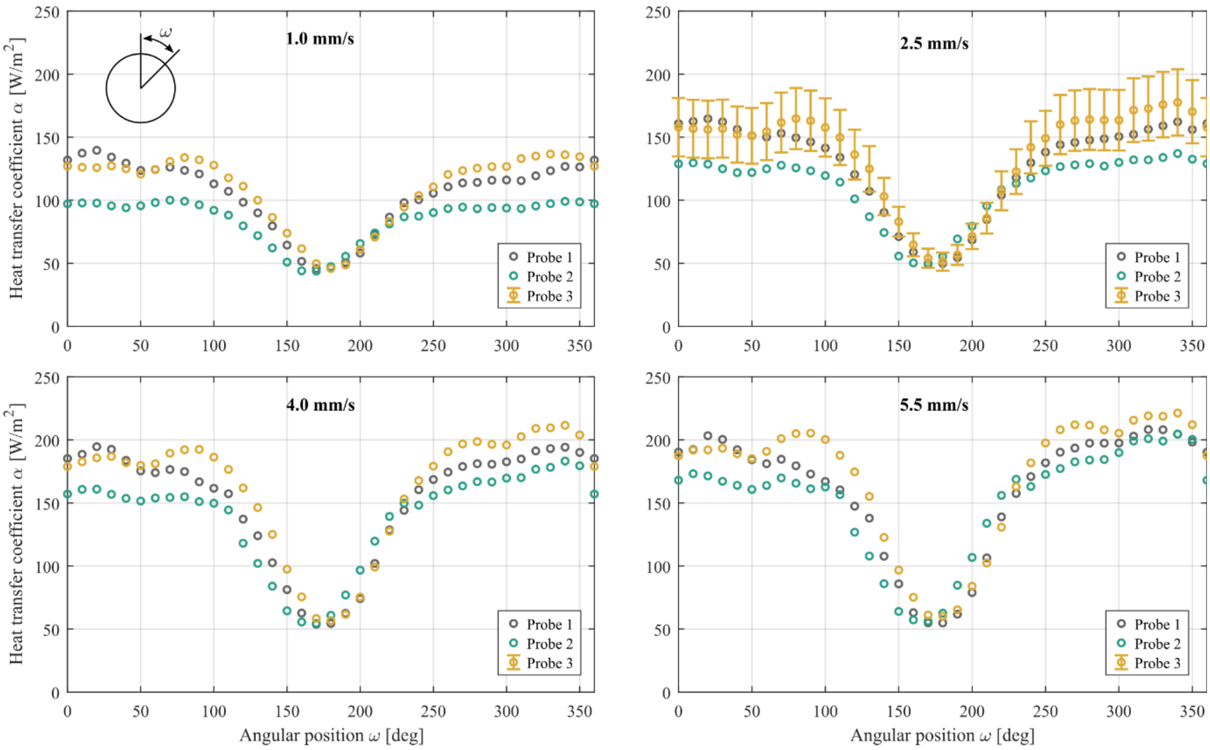

Fig. 6 Measured HTCs α and error bars as a function of angular wall position ω for different probe positions and outlet velocities.

Some curves suggest a slight peak towards the flank of the tube ($\omega = 90°$), which can be ascribed to increased convection and partial mixing that takes place in the converging region between two adjacent tubes. In contrast, after passing the bottleneck, heat transfer drops significantly. As was outlined in

Section 2, this is where particles begin to detach from the wall and increased voidage leads to an increased thermal resistance (see Eq. (7)). A minimum is reached just below the tube where the void zone is at its largest. Here, the bulk is completely detached from the wall and heat transfer is dominated by radiation and natural convection of the air. It is noteworthy, that coefficients at this point seems to stay unaffected by the flow velocity. The minimum remains at approximately $50\,\mathrm{W/m^2}$, while heat transfer curves otherwise rise collectively with higher velocities.

When comparing curves at different probe positions in the mockup, it can be observed that probe 1 and probe 3 show similar trends at similar levels. Heat transfer at probe 2, on the other hand, is clearly reduced. The reason for this are lower driving temperature gradients caused by the thermal boundary layer that was passed on from probe 1.

As for the error bars in Fig. 6, calculations were based on the maximum measurement uncertainty assumption using the data provided in Table 2. The largest fraction of the uncertainties in Fig. 6 originated from the engineering tolerance of the thickness of the foil, which the manufacturer stated at 10%.

Fig. 7 illustrates the comparison of experimental results with CFD simulations. Generally, simulated HTCs are in good agreement with the experimental values. Most discrepancies occur at the top of the tubes. In this region, it seems that simulations overestimate the insulation effect of the stagnation zone, especially at higher velocities. While according to simulations the heat transfer is significantly impaired, experiments show a rather horizontal trend. Although particle motion is indeed reduced within the stagnant zone, in practice, a constant replacement still takes place and even scales with the average bulk velocity.

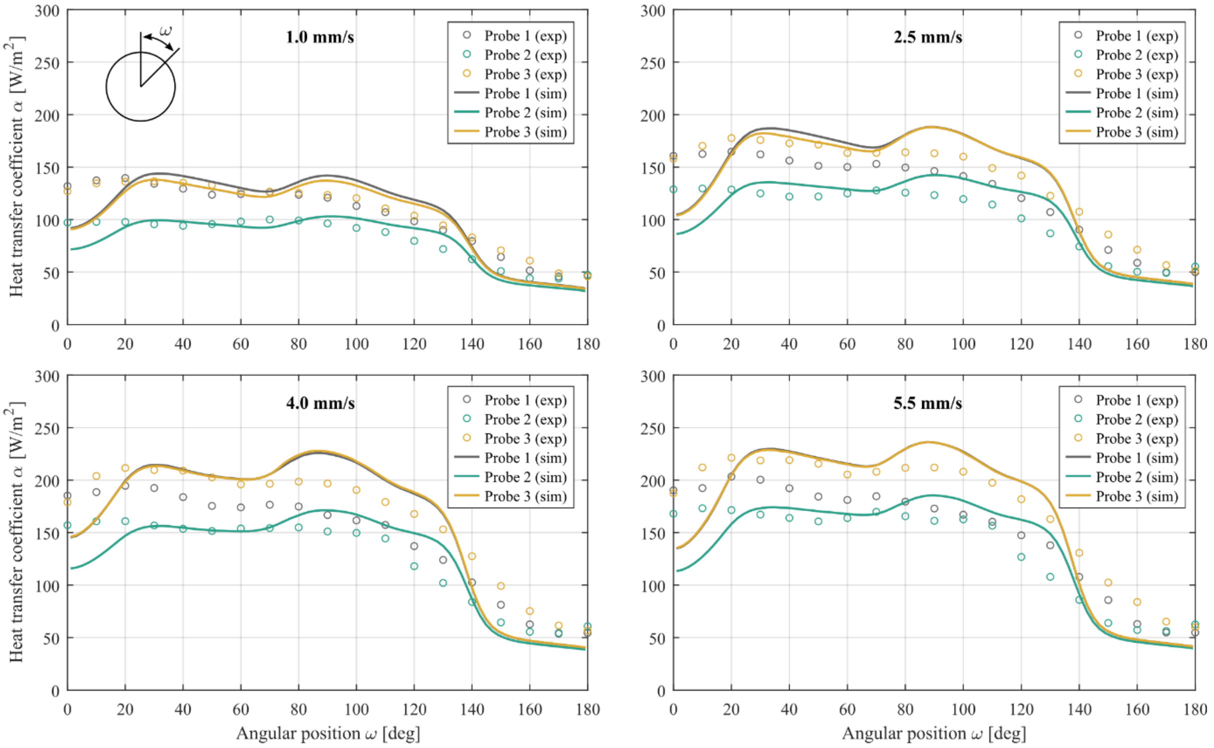

Fig. 7 Comparison of simulated and experimental HTCs α as a function of angular wall position ω for different probe positions and outlet velocities.

Notable differences are observable in the diverging region past the bottleneck ($\omega > 90°$). Once past the narrowest point, measured HTCs decrease more or less steadily until the void zone is reached, where heat transfer quickly levels off at the global minimum. At first, simulations follow a similar trend with only a slight overshot near the flank but then suddenly drop. This rapid decline was predetermined by Eq. (6), which in its current form seems to overestimate the effect of particle separation.

As the simulation domain is symmetrical, results for probe 1 and 3 are basically identical at higher velocities, while at lower velocities they diverge slightly. This is plausible because at lower velocities, the heat transfer at probe 3 starts to be affected by the thermal boundary layer of opposite tubes — in this case probe 1 and probe 2 (see Fig. 5). Consequently, heat transfer at probe 3 is moderately lower than at probe 1.

Knowing the distribution of local HTCs and wall temperatures along the tube circumference can be useful information to study different tube designs or to assess the risk of thermal stresses. Nevertheless, from a design point of view, the average HTC at each tube is a more useful parameter. Fig. 8 illustrates the area weighted HTC, $\bar{\alpha}$, in Eq. (13) at different bulk velocities.

$$\bar{\alpha} = \frac{1}{A_{tube}} \int_0^A \alpha(\omega)\, dA \tag{13}$$

Once more, it can be observed that simulations match the test results. What stands out when looking merely at the experimental curves (dashed lines) is that there are obvious differences between probe 1 and 3. This is somehow surprising because if the flow field was perfectly symmetrical and the heat flux from the probes identical, heat transfer rates would also be the same, especially at higher velocities. Following from this, it is suspected that during the time of measurement the flow field was in fact not perfectly symmetrical.

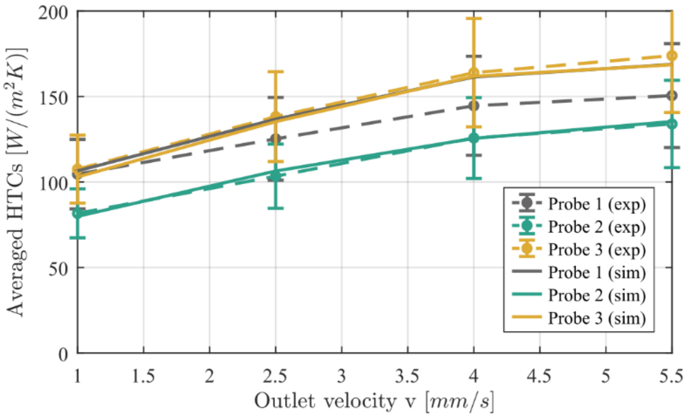

Fig. 8 Area weighted HTC for different probe positions and outlet velocities

This hypothesis is supported by the PIV results illustrated in Fig. 9. The images prove that a significant fraction of the mass flux is actually located along the baffle plates near the casing. More importantly, there can also be seen differences of flow patterns around different tubes. This might suggest that the assumption of flow field symmetry doesn’t hold in practice. Furthermore, it seems that these differences are not random: The closer to the lateral baffle plates, the higher the velocities. This could explain why less heat is transferred at probe 1, which is located in the very centre, when compared to probe 3, which is located closer to the wall.

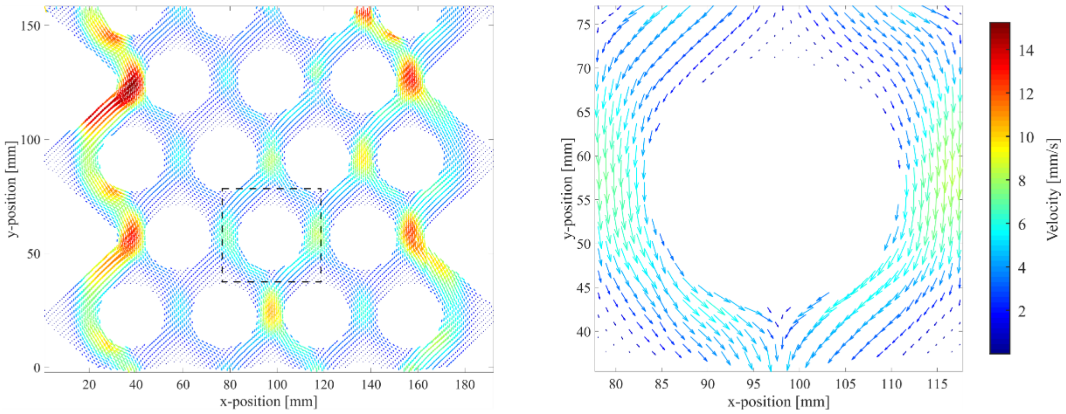

Fig. 9 Granular velocity field based on particle image velocimetry in the region demonstrated in Fig. 3.

Finally, it is worth discussing the magnitude of transferred heat. According to Fig. 9, measured HTCs obtained in this study lie in the range of 80 to 150 W/m2. This range corresponds to results from Takeuchi [32] ($50 < \bar{\alpha} < 100$ W/m2) and Bartsch [25] (($100 < \bar{\alpha} < 150$ W/m2) who both applied the same experimental method studying similar bulk material and velocities. It should be reiterated that in our experiments we applied a constant heat flux, while heat transfer under more realistic operating conditions would rather be described with a temperature boundary condition. More importantly, here, heat transfer took place at relatively low temperatures below 130 °C. At higher temperatures heat transfer by radiation becomes increasingly prevalent both in the bulk and at the tube wall, so higher HTCs could be expected in a power plant that operate at temperatures above 1000 °C. This can in part be seen in Baumann [33], who performed experiments at inlet temperatures of 600°C and obtained overall HTCs of 160–290 W/m2 at the first tube row.

5 Summary and conclusion

In this article, we validated a set of thermal models to simulate the heat transfer in heat exchangers with horizontal tubes. To resolve the local heat transfer coefficient along the circumference of tubes, we adopted the method of Takeuchi [32], which uses specially prepared measuring probes. After performing measurements at discharge velocities of 1.0, 2.5, 4.0 and 5.5 mm/s, good agreement could be observed between simulations and experimental results.

Most differences appeared at the upper part of the tube where the stagnant zone is located. In the stagnant zone heat transfer is diminished due to impaired particle motion and, hence, reduced convection. Simulations seem to overestimate this effect. Moreover, the modelling of the void zone and separation of particles at the lower part of the tube should also be improved. The decline of heat transfer rates towards this region was in practice more moderate than suggested by simulations. Nevertheless, on balance, CFD results proved to be very accurate. Both the measured and simulated area weighted heat transfer coefficients were very similar.

With the described method, it was possible to demonstrate that the presented thermal model is indeed able to predict the complex heat transfer characteristics found in shell-and-tube moving bed heat exchangers. But, there remain certain caveats to bear in mind. First, measurements in this study were based on a constant heat flux boundary condition. While it was easier to realize tests by using a heated foil, in reality, heating or cooling the bulk with a heat transfer fluid would better mimic the operating conditions found in a power plant. Second, the temperature level at which heat transfer took place in the tests was well below those that such devices are actually designed for. The temperature has great influence on the thermophysical properties of the bulk and the radiation levels. These effects could not be captured by the experiment.

In conclusion, the method described in this work was a useful way to proof the validity of our simulation tool, but the presented heat transfer coefficients cannot necessarily be compared to those found during plant operation.

Acknowledgements

References

[1] Albrecht KJ, Ho CK. High-temperature flow testing and heat transfer for a moving packed-bed particle/sCO2 heat exchanger. Conference High-temperature flow testing and heat transfer for a moving packed-bed particle/sCO2 heat exchanger, vol. 2033.
[2] Albrecht KJ, Ho CK. Design and operating considerations for a shell-and-plate, moving packed-bed, particle-to-sCO2 heat exchanger. Solar Energy. 2019;178:331-40.
[3] Ho CK, Albrecht KJ, Yue L, Mills B, Sment JN, Christian J, et al. Overview and Design Basis for the Gen 3 Particle Pilot Plant (G3P3). Conference Overview and Design Basis for the Gen 3 Particle Pilot Plant (G3P3), Bellevue, WA, USA.
[4] Baumann T, Zunft S, Tamme R. Moving Bed Heat Exchangers for Use With Heat Storage in Concentrating Solar Plants: A Multiphase Model. Heat Transfer Engineering. 2014;35(3):224-31.
[5] Baumann T, Zunft S, Knödler P. Moving Bed Heat Exchanger for solar-driven steam cycles: Experimental validation of multiphase CFD simulations. IEA-ECES-Greenstock. Peking, China2015.
[6] Niegsch J, Könecke D, Weinspach P-M. Heat transfer and flow of bulk solids in a moving bed. Chemical Engineering and Processing. 1994;33:73-89.

[7] HelioHeat GmbH. HIFLEX - High Storage Density Solar Power Plant for Flexible Energy Systems. 2021.
[8] Albrecht KJ, Ho CK. Heat Transfer Models of Moving Packed-Bed Particle-to-sCO2 Heat Exchangers. Journal of Solar Energy Engineering. 2018;141(3).
[9] Baumann T, Zunft S. Properties of granular materials as heat transfer and storage medium in CSP application. Solar Energy Materials and Solar Cells. 2015;143:38-47.
[10] Eschner A. Industrial Refractories. In: VDI-Gesellschaft Verfahrenstechnik und Chemieingenieurwesen (GVC), editor. VDI Heat Atlas. Second Edition ed. Düsseldorf, Germany: Springer; 2010. p. 581-90.
[11] Guo Z, Zhang S, Tian X, Yang J, Wang Q. Numerical investigation of tube oscillation in gravity-driven granular flow with heat transfer by discrete element method. Energy. 2020;207.
[12] Guo Z, Tian X, Yang J, Shi T, Wang Q. Comparison of Heat Transfer in Gravity-Driven Granular Flow near Different Surfaces. Journal of Thermal Science. 2020.
[13] Tian X, Yang J, Guo Z, Wang Q, Sunden B. Numerical Study of Heat Transfer in Gravity-Driven Particle Flow around Tubes with Different Shapes. Energies. 2020;13(8).
[14] Bartsch P, Zunft S. Numerical investigation of dense granular flow around horizontal tubes: Qualification of CFD model with validated DEM model. Solar Energy. 2019;182:298-303.
[15] Bartsch P, Zunft S. Granular flow around the horizontal tubes of a particle heat exchanger: DEM-simulation and experimental validation. Solar Energy. 2019;182:48-56.
[16] ANSYS Inc. Multiphase Flows. Fluent Theory Guide2021.
[17] Zehner P, Schlünder EU. Wärmeleitfähigkeit von Schüttungen bei mäßigen Temperaturen. Chemie Ingenieur Technik. 1970;42(14):933-41.
[18] Zehner P, Schlünder EU. Einfluß der Wärmestrahlung und des Druckes auf den Wärmetransport in nicht durchströmten Schüttungen. Chemie Ingenieur Technik. 1972;44(23):1303-8.
[19] van Antwerpen W, du Toit CG, Rousseau PG. A review of correlations to model the packing structure and effective thermal conductivity in packed beds of mono-sized spherical particles. Nuclear Engineering and Design. 2010;240(7):1803-18.
[20] Grobbel J, Brendelberger S, Sattler C, Pitz-Paal R. Heat transfer in a directly irradiated ceria particle bed under vacuum conditions. Solar Energy. 2017;158:737-45.
[21] Kuipers JAM, Prins W, van Swaaij WPM. Numerical Calculation of Wall-to-Bed HeatTransfer Coefficients in Gas-Fluidized Beds. AIChE Journal. 1992;38(7):1079-91.
[22] Gunn DJ. TRANSFER OF HEAT OR MASS TO PARTICLES IN FIXED AND FLUIDISED BEDS. Int J Heat Mass Transfer. 1978;21:467-76.
[23] Botterill JSM, Denloye AOO. A theoretical model of heat transfer to a packed or quiescent fluidized bed. Chemical Engineering Science. 1978;33(4):509-15.
[24] Tsotsas E. Heat transfer from a wall to stagnant and mechanically agitated beds. VDI Heat Atlas. 2nd Edition ed: Springer; 2010. p. 1311-26.
[25] Bartsch P. Entwicklung neuer Modelle zur Beschreibung von Schüttgutströmungen in Wanderbettwärmeübertragern [Doctoral]. Stuttgart: Universität Stuttgart, 2020.
[26] Busch A, Johansen ST. On the validity of the two-fluid-KTGF approach for dense gravity-driven granular flows as implemented in ANSYS Fluent R17.2. Powder Technology. 2020;364:429-56.
[27] Niegsch J. Schüttgutbewegung und Wärmeübergang im Wanderbett. Dortmund: Universität Dortmund, 1993.
[28] Churchill SW, Chu HHS. Correlating equations for laminar and turbulent free convection from a vertical plate. International Journal of Heat and Mass Transfer. 1975;18(11):1323-9.
[29] Span R. Properties of Dry Air. In: VDI-Gesellschaft Verfahrenstechnik und Chemieingenieurwesen (GVC), editor. VDI Heat Atlas. Ruhr-Universität Bochum: Springer; 2010.
[30] Kabelac S, Vortmeyer D. Radiation of Surfaces. VDI Heat Atlas. 2nd Edition ed: Springer; 2010. p. 947-59.
[31] Baumann T, Zunft S. A MOVING BED HEAT EXCHANGER FOR SOLAR THERMAL POWER APPLICATIONS: EXPERIMENTAL INVESTIGATION OF GRANULAR FLOW AND THERMAL PERFORMANCE. 8th World Conference on Experimental Heat Transfer, Fluid Mechanics, and Thermodynamics. Lissabon, Portugal2013.

[32] Takeuchi H. Particles Flow Patterns and Local Heat Transfer Around Tube in Moving Bed. AIChE Journal. 1996;42(6):1621-6.

[33] Baumann T. Wärmeauskopplung aus heißen Partikelschüttungen zur Dampferzeugung. Stuttgart: Universität Stuttgart, 2014.